Journal of Ovarian Research

RESEARCH

Open Access

Circulating plasma gelsolin and MRI-based radiomics as biomarkers of platinum resistance in epithelial ovarian cancer: building a multiparameteric prediction algorithm

Emma Gerber[1,2,3,4†], Rahul Singh[4†], Cheuk Nam Hwang[4], Lei Cai[5], Alice S. T. Wong[5], Dylan Burger[1,2], Karen K. L. Chan[3*], Benjamin K. Tsang[1,2,6*] and Elaine Y. P. Lee[4*]

Abstract

Background Resistance to platinum-based chemotherapy in epithelial ovarian cancer (EOC) patients is a barrier to disease management. Currently, there are no biomarkers to predict chemoresistance. Plasma gelsolin (pGSN) in circulating small extracellular vesicles (sEV) has previously been shown to predict chemoresistance in treatment-naïve EOC. Here, we expand upon sEV-pGSN as biomarker by incorporating MRI-based radiomics to improve the prediction of chemoresistance in EOC patients.

Methods In this retrospective study, we used serum from 37 EOC patients with paired baseline MRI from the University of Hong Kong between 2016 and 2020. sEVs were isolated from serum samples using differential centrifugation and characterized by nanoparticle tracking analysis, western blotting, and transmission electron microscopy. Total pGSN and sEV-pGSN were quantified using sandwich ELISA. Radiomic features were extracted from the primary tumour on the MRI T2-weighted images (T2), apparent diffusion coefficient (ADC) maps ($b = 0,400,800$ s/mm^2), and post-contrast images (PC). Highly correlated features (Spearman correlation coefficient of > 0.85) were removed and repeatable features selected using elastic-net regression. Grid-search 10-fold SCVs was utilized to optimize the hyper-parameters of the K-Nearest Neighbor (ADC and T2 + ADC + PC), Gaussian Naïve Bayes (T2), Linear Discriminant Analysis (PC), and Support Vector Machine (T2 + ADC) classifiers to build the prediction models, including total and sEV-pGSN.

†Emma Gerber and Rahul Singh contributed equally to this work.

*Correspondence:
Karen K. L. Chan
kklchan@hku.hk
Benjamin K. Tsang
btsang@ohri.ca
Elaine Y. P. Lee
eyplee77@hku.hk

Full list of author information is available at the end of the article

Results Among the 37 EOC patients (56±11 years old), 65% presented at advanced stage (FIGO III-IV, $n=24$). Thirty-one patients were chemosensitive and six were chemoresistant (progression free interval < 12 months). The combination of total and sEV-pGSN could predict chemoresistance (AUC = 0.591), however the inclusion of MRI radiomic features improved the test performance. The prediction model based on total pGSN, sEV-pGSN, and 4 selected T2 radiomic features showed the best performance in predicting chemoresponsiveness with the following mean performance metrics: AUC (0.973), sensitivity (0.833), specificity (0.968) and accuracy (0.946).

Conclusion Our prediction model using total and sEV-pGSN and T2 features demonstrated excellent diagnostic ability in predicting chemoresistance in EOC patients, which could be used to facilitate alternate tailored therapeutics. Building on this work in larger multicentre studies will further validate these findings and clarify the utility of a combined radiomics/EV biomarker approach to chemoresistance prediction in EOC.

Keywords Epithelial ovarian cancer, Small extracellular vesicles, Plasma gelsolin, Magnetic resonance imaging, Radiomics, Chemoresistance, Biomarkers

Background

Platinum-based chemotherapy is part of the first-line treatment for epithelial ovarian cancer (EOC) [1]. Although it is expected that most patients will eventually develop resistance to chemotherapy [2], there is no clinical biomarker to guide clinical management of the disease. CA125 is the biomarker used to monitor disease progression and platinum sensitivity during and after treatment [3], but it is unable to predict responsiveness in chemo-naïve patients. While many studies investigating methods to predict chemoresistance have been reported in the context of response monitoring during treatment [4], this information is too late for clinical management. Rather, we should be aiming to prevent subjecting non-responsive patients to these toxic substances with systemic effects that compromise quality of life [5]. By identifying biomarkers of platinum-resistance in chemo-naïve patients, we hope to enable the ability for physicians to offer individualized treatment options, thus improving their survival outcomes.

The use of liquid biopsy biomarkers offers useful information in personalized care for cancer patients through minimally invasive sample collection [6]. Such biomarkers are particularly of interest for cancer diagnosis, progression monitoring, and guiding therapeutic approaches [6]. Our group has highlighted plasma gelsolin (pGSN), a secreted actin binding protein, as a circulating biomarker of EOC. We have shown its utility in predicting stage of disease and residual disease, as well as chemoresponsiveness in chemo-naïve patients [7, 8]. At the cellular level, pGSN is secreted from chemoresistant EOC cells in small extracellular vesicles (sEVs), which confer resistance in neighbouring chemosensitive EOC cells [9]. Indeed, we were able to demonstrate that when circulating sEV-pGSN was considered alongside total circulating pGSN, that they contributed to efficient prediction of chemoresponsiveness (sensitivity of 74% and specificity 72%) [8].

Diagnostic imaging, such as magnetic resonance imaging (MRI), computed tomography (CT), and ultrasound, is part of the standard diagnostic algorithm for EOC patients. These offer valuable information on the characteristics of ovarian masses, including size, presence of necrotic tissue, and ascites [10]. Radiomics is a field of study that takes advantage of this whole tumour imaging. From these images, quantitative features are extracted, and the resulting data is thought to reflect the pathophysiology of the tissue [11]. Predictive models based on radiomic features have been shown to differentiate type I and type II EOC tumours [12]. and high-grade vs. non-high-grade serous adenocarcinoma [13]. This highlights the utility of radiomics to distinguish between tumour differences at a molecular level (i.e., subtypes of EOC) using macroscopic imaging features. Whether MRI-based radiomics can assist in the prediction of chemoresistance in EOC remains to be shown.

In this study, we have aimed to combine MRI-based radiomic features with the pre-established circulating total and sEV-pGSN to improve upon the prediction of chemoresistance in treatment-naïve EOC patients.

Materials and methods

Patient samples

Serum samples for this retrospective study were collected from patients diagnosed with EOC at Queen Mary Hospital in Hong Kong between 2016 and 2020. Serum collection was approved by the designated research ethics board (IRB # UW11-298) and patients provided written informed consent for their participation. Clotted blood samples were centrifuged at 2000 rpm at 20 °C (Thermo Scientific, Sorvall ST 40R) for 20 min. The serum was transferred to a 2mL tube and centrifuged again at 8000 rpm at 4 °C (Hitachi, CT15RE) for 10 min. The resulting serum was stored at −20 °C.

MRI scans from the patients whose serum had been collected were retrieved from the University of Hong Kong Department of Diagnostic Radiology database. These scans were obtained at baseline, before the patients had undergone any treatment. Examinations were

performed on a 3.0T-MRI platform with the same scanning parameters, which included: T2-weighted imaging (T2), diffusion weighted imaging [DWI; $b = 0$, 400, and 800 s/mm^2 were used to construct an apparent diffusion coefficient (ADC) map for analysis], and post-contrast imaging (PC) (Table 1). Curation of these scans for the purpose of this study was approved by the designated research ethics board (IRB #UW18-607).

Clinical information collected included histologic subtype, FIGO stage, progression free survival, overall survival, CA125 at diagnosis, chemotherapy, and surgical information. BRCA testing was only performed for 16 of the 37 patients included in the cohort. Other genetic testing, including TP53 and other homologous recombination deficiency (HRD) was not performed routinely at the time that samples were collected, therefore that information is not available for this group. Likewise, KELIM scores were not recorded in Hong Kong during the study period, therefore we were unable to compare our prediction algorithm to this predictor. Overall survival and progression free survival (PFS) was defined as the time between diagnosis (based on the date of imaging) and death or recurrence, respectively. Recurrence was defined based on increasing levels of CA125. For the purposes of this study, we stratified patients into chemosensitive and chemoresistant groups based on a PFS of 12 months, where those who experienced recurrence prior to 12 months were considered chemoresistant.

Small EV isolation

All phosphate buffered saline (PBS) used in the isolation of extracellular vesicles was first centrifuged at 100,000 g for 2 h and the top 90% fraction was saved for use. 100μL of serum from each patient was diluted in 400μL of PBS and mixed well by pipetting. Samples were centrifuged at 20,000 g for 20 min to pellet any cellular debris and large EVs. The supernatant was reserved for the following centrifugation step and the pellet was discarded. The supernatant was transferred to a micro-ultracentrifuge tube and an additional 500uL of PBS was added. Samples were then centrifuged at 100,000 g for 90 min using the CP100NX ultracentrifuge with the P50A3 rotor from Himac. Following centrifugation, the supernatant was carefully removed and discarded and the pellet was resuspended in 500uL of PBS. All samples were stored at −80 °C.

Table 1 Summary of MRI scanning parameters. TR: repetition time. TE: echo time. FOV: field of view. T2W1: T2-weighted imaging. DWI: diffusion weighted imaged

Sequences	Axial T2W1	DWI	Contrast-enhanced 3D T1W1
Coverage	Diaphragm to the groin	Diaphragm to the groin	Diaphragm to the groin
TR/TE (msec)	622/10	1210/53	3/1.4
FOV (cm)	1200×1200	480×480	640×640
Matrix size	580×438	160×157	248×245
Slice Thickness (mm)	4	4	3
Receiver Bandwidth (kHz)	218	3004	724

Western blot

Isolated sEVs were lysed prior to western blot analysis. To do so, equal volumes of sEVs in PBS and 2X RIPA buffer (Millipore cat. # 20–188) were combined and incubated on ice for 30 min. Samples were then sonicated using a probe sonicator and incubated on ice for another 15 min. The samples were centrifuged at 12,000 g for 30 min and the supernatant was reserved for western blot analysis. Samples were prepared in sample loading buffer (Cell Signaling Technology 3X Blue Loading Buffer and 30X reducing reagents, cat.#56036S) and heated to 100 °C for 5 min prior to loading in a 10% SDS-acrylamide gel. A molecular weight ladder was included (BioRad, Precision Plus Protein Dual Color Standards, cat.#1610374). Electrophoresis was carried out at 100 V for 30 min followed by 60 min at 120 V. BioRad 10X Tris/Glycine/SDS buffer was used as a running buffer (cat.#1610772). For the transfer, BioRad 10X Tris/Glycine buffer (cat.#1610771) was prepared with 20% methanol. PVDF membrane (BioRad, Immuno-blot PVDF membrane, cat.#1620177) was activated in methanol for 30 s and then rinsed in water. The activated membrane, acrylamide gel, sponges, and filter paper were soaked in transfer buffer prior to the transfer. The wet transfer was run at 110 V for 90 min on ice and at 4 °C. The resulting membrane was stained with Ponceau stain and rinsed with water to assess the success of the protein transfer. The membrane was then blocked with 5% bovine serum albumin (BSA) prepared in tris-buffered saline with Tween-20 (TBST) for 1 h at room temperature. Finally, the proteins of interested were probed with primary antibodies overnight at 4 °C. The following day, the membrane was washed two times for 5 min with TBST and then probed with the secondary antibody for 1 h at room temperature. A final washing was performed three times for 15 min with TBST. The membrane was soaked in ECL (BioRad, Clarity Western ECL Substrate, cat.#1705061) for 1 min. Blots were developed using X-ray film in a dark room. The antibodies used included the following: Calnexin, 1/1000 prepared in 5% BSA in TBST, negative sEV marker (Cell Signalling Technology, cat.#2679). CD9, 1/1000 in 3% BSA in phosphate-buffered saline with Tween-20 (PBST), sEV marker (abcam, cat.# ab236630). TSG101, 1/1000 in 3% BSA in PBST, sEV marker (abcam, cat.#ab125011). B-actin, cytosolic sEV marker (Invitrogen, cat.#MA5-15739). Secondary antibodies included: Donkey anti-rabbit, 1/2000 in 5% BSA in TBST (Cytiva, cat.# NA934). Sheep anti-mouse,

1/2000 in 5% BSA in TBST (Cytiva, cat. #NA931). See Fig. 1A.

Nanoparticle tracking analysis

To further validate the isolation of sEVs, we performed nanoparticle tracking analysis (NTA) to evaluate particle size. Briefly, isolated sEVs were diluted in ddH_2O to a level that permitted a view of 100–200 particles per frame using the ZetaView nanoparticle tracking system (Particle Metrix, Germany) [14, 15]. We used size-mode analysis with ZetaView software (version 8.02.12) following calibration with polystyrene beads (105 and 500 nm). Samples were analyzed at a minimum of 10 camera positions with 2-second video length at 23 °C. See Fig. 1B.

Transmission electron microscopy

Transmission electron microscopy (TEM) was used to further visualize the isolated sEVs. Here, 10µL of the resuspended sEVs were added to a 400-mesh copper grid with carbon-coated formvar film. After a 2-minute incubation, the extra liquid was removed, and the grid was briefly placed on 10µL of uranyl acetate. This was then washed twice with 100µL of MilliQ water. The dried EVs on the grid were visualized using a Philips CM100 microscope. EVs were identified as structures with a lipid bilayer and a size between 100 and 200 nm. See Fig. 1C.

Enzyme-linked immunosorbent assay

To quantify total and sEV-pGSN from patient serum samples, we used sandwich enzyme-linked immunosorbent assay (ELISA). The human soluble plasma gelsolin sandwich ELISA kit from Aviscera Bioscience Inc. (SK00384-01) was used as per the manufacturer's instructions. To measure total pGSN, samples were diluted by a factor of 15,000. For sEV-pGSN, lysed samples were and diluted by a factor of 100. Concentrations were measured using a standard curve with seven points (0.78-50ug/mL) in singlet and the blank optical density (OD) was subtracted from all samples. Intra-assay and inter-assay precision are 4–6% and 4–9%, respectively. Total pGSN concentrations are reported in µg/mL while sEV-pGSN concentrations are reported in ng/mL.

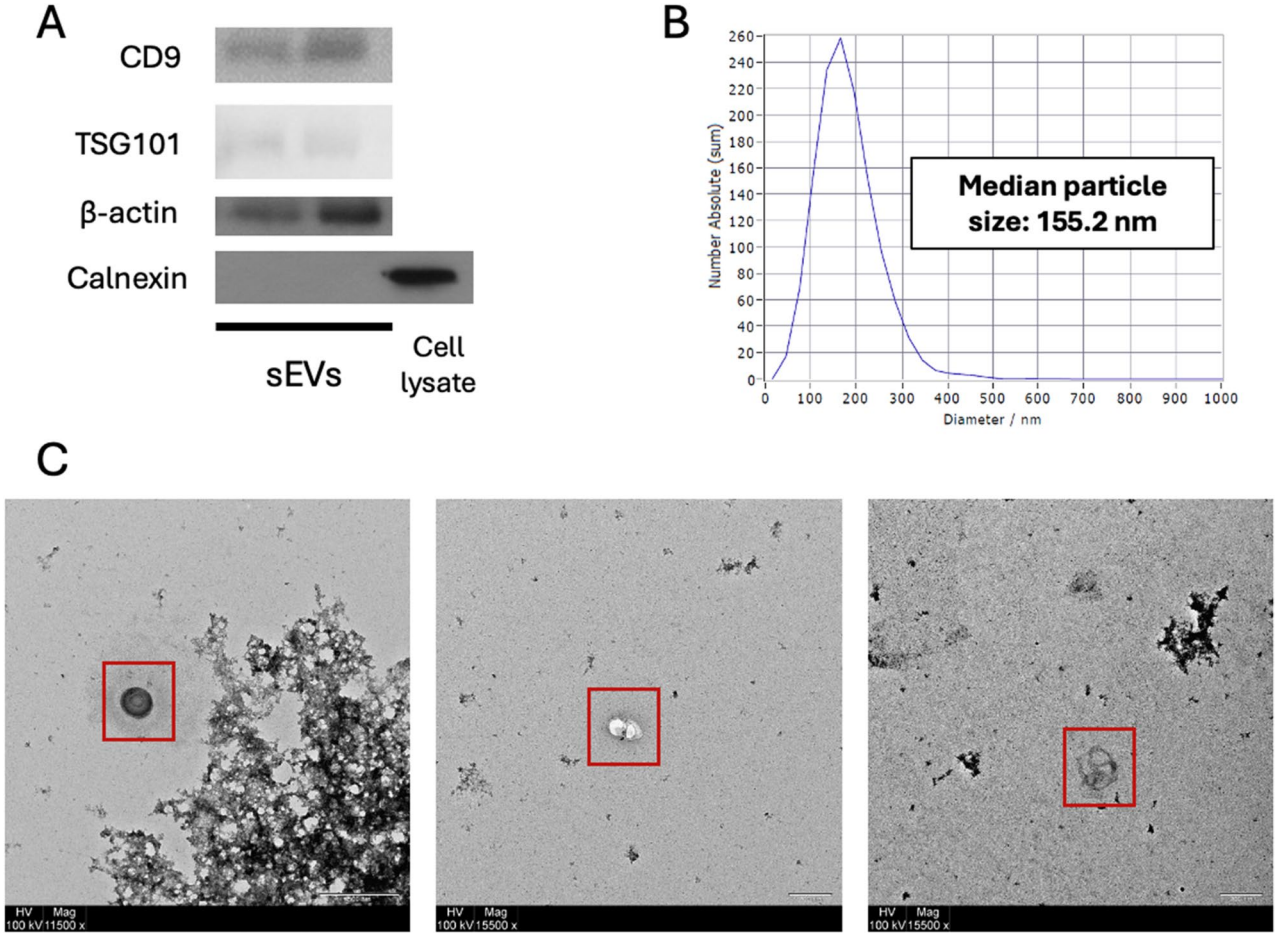

Fig. 1 Characterization of sEVs. **A** Western plot of isolated sEVs. CD9 and TSG101 are sEV markers. β-actin is a cytosolic marker to confirm the isolation of intact EVs. Calnexin is a negative marker and should not be detected in EVs. **B** Size distribution curve of sEVs from nanoparticle tracking analysis. The expected size range of sEVs is 30–150 nm. **C** Electron transmission microscopy images to visualize sEVs in the sample

Tumour segmentation on MR images

Segmentation, or outlining of the tumour on the MRI images, was performed manually using the segmentation tool on ITK-SNAP [16] (version 4.0.1; http://www.itksnap.org/). This was done for each scan from all three MRI sequences. Segmentations were reviewed and confirmed by E.L., a board-certified radiologist with more than 15 years post-fellowship experience and clinical expertise in gynaecologic imaging. The volumes of interest (VOIs) were used for subsequent feature extraction.

Image perturbation

Due to a small sample size, we incorporated controlled image perturbations on both the images and their corresponding masks to synthetically increase the sample size. The objective of this step was to improve efficacy of feature selection for subsequent modeling. Four different types of perturbations were applied: rotation, scaling, shear, and zoom.

Rotation was applied along the z-axis within the axial (x, y) plane at angles of ±5° and ±10°, generating four variations per image. This was intended to simulate minor orientation shifts that could occur due to variability in patient positioning or acquisition protocols. Scaling transformations, with factors of 0.8, 0.9, 1.1, and 1.2, adjusted the image size, mimicking potential alterations in spatial resolution or voxel dimensions during acquisition. Shear transformations, with shear factors of 0.1 and −0.1, introduced geometric distortions by skewing the coordinate grid, simulating minor deformations due to equipment inconsistencies or motion. Zoom perturbations, applied with factors of 0.9 and 1.1, modified the focal scale, simulating changes in the field of view that may arise from variations in scanning protocols. With 12 image perturbations plus the original image, this increased our sample size 13-fold for each sequence.

Radiomics feature extraction

The radiomics features were extracted from the VOIs of the original images and their corresponding perturbed images using the open-source PyRadiomics package (version 3.0.1; http://www.radiomics.io/pyradiomics.html) [17], which is Image Biomarker Standardization Initiative compliant [18]. For each MRI sequence, radiomic features were extracted using a bin width of 25, with seven distinct feature classes. These classes included shape, first-order statistics, gray-level co-occurrence matrix (GLCM), gray-level size zone matrix (GLSZM), gray-level run-length matrix (GLRLM), gray-level dependence matrix (GLDM), and neighboring gray-tone difference matrix (NGTDM) features. Beyond these primary features, advanced texture features were generated through the application of Laplacian of Gaussian filters (with σ values ranging from 1 to 5) and wavelet transformations, which yielded eight image decompositions. PyRadiomics extracted a total of 1151 features from each MRI sequence for every patient. After eliminating irrelevant features, 1106 radiomics features remained for subsequent analysis. These features were standardized using the z-score method before feature selection to assure a similar scale amongst all features.

Feature reduction and selection

Once the radiomic features were extracted, highly correlated features were eliminated by Spearman rank correlation using threshold of 0.85. This step led to the retention of 68, 55, and 56 features for T2, ADC, and PC images, respectively. To identify highly repeated and reproducible features that could potentially contribute to the prediction of chemoresistance, we employed elastic net regression, which was conducted 100 times with 5-fold cross-validation, yielding 500 iterations. Features that were selected in over 300 of these iterations were retained for the subsequent step of feature selection. Thereafter, the Mann-Whitney U test was conducted to evaluate the statistical significance of the retained features, with a significance threshold set at $p < 0.05$. This approach resulted in the selection of 4, 5, and 4 significant features for the T2, ADC, and PC sequences, respectively. The feature reduction and selection steps were also applied to the combined sequences. The initially extracted 1106 radiomics features from each imaging sequence were pooled for joint feature reduction and selection. For the T2 + ADC model, 11 statistically significant features (6 from T2 and 5 from ADC) were identified, while the T2 + ADC + PC model yielded 6 features (2 from T2, 3 from ADC, and 1 from PC). The sEV-pGSN, as well as predetermined CA125 were also subjected to Mann-Whitney U test. Both measures of pGSN were found to be statistically significant, while CA125 was not. Consequently, CA125 was excluded from the following predictive modelling.

Machine learning-based model building

We trained and evaluated the performance of different machine learning (ML) base classifiers, including Logistic Regression (LR), K-Nearest Neighbors (KNN), Gaussian Naive Bayes (GNB), Support Vector Machines (SVMs) and Linear Discriminant Analysis (LDA) using 10-fold cross validation (CV) for predicting chemoresponsiveness in EOC patients. Each classifier was trained on every MRI sequence and combined sequences utilized respective statistically significant features including total pGSN and sEV-pGSN. The predictive performance was quantified by evaluating the AUC, accuracy, sensitivity, and specificity. To improve the predictive performance and avoid potential overfitting, Grid-search CV was applied in the best performing base classifier, which searches the

hyperparameter space for optimal combinations of the hyperparameters.

Results

Patient demographics

In this cohort of patients, we had paired serum samples and MRI scans from 37 patients with EOC. All patients underwent carboplatin chemotherapy, and serum samples and MRI were collected prior to any treatment. The two histologic subtypes accounting for most cases were clear cell carcinoma (CCC, 38%) and high-grade serous carcinoma (HGSC, 27%). Approximately 2/3 of patients had late-stage cancer, including 43% and 22% with FIGO stage 3 and 4, respectively. BRCA testing was only performed for 16 of the 37 patients, of which 5 tested positive. Chemoresponsiveness was stratified by a PFS of 12 months, in which patients who experienced recurrence before 12 months were considered resistant to chemotherapy, while those with recurrence after 12 months were chemosensitive. For this group, 84% of patients were chemosensitive and 16% chemoresistant. All but one patient underwent cytoreductive surgery. The patient who did not receive surgery had stage 3 clear cell carcinoma and experienced disease progression on chemotherapy. Therefore, this was not followed by cytoreduction. A breakdown of these patient characteristics can be seen in Table 2.

Table 2 Patient demographics. FIGO: international federation of gynecology and obstetrics

Characteristics	Number (*n*=37)	Percentage (%)
Age (range: 31–82, mean 56)		
<56	18	48
≥56	19	52
Histopathologic Subtype		
High grade serous	10	27
Low grade serous	0	0
Endometrioid	5	13.5
Mucinous	1	3
Clear cell	14	38
Mixed	2	5
Other	5	13.5
FIGO Stage		
1	10	27
2	3	8
3	16	43
4	8	22
Progression Free Survival		
< 12 months	6	16
>12 months	31	84
Chemotherapy		
Neo-adjuvant	12	32
Adjuvant	25	68
Response to chemotherapy		
Complete response	32	86
Progressive disease	3	8
Stable disease	1	3
Not reported	1	3
Cytoreductive surgery		
Surgery	36	97
No surgery	1	3
Surgical outcome		
Complete cytoreduction	28	75.5
Residual disease	8	21.5
Not applicable	1	3

Total and sEV-pGSN levels in chemoresistant patients

To compare pGSN between chemoresistant and chemosensitive patients, we quantified total and sEV-pGSN in the serum samples of all patients. We found that total pGSN tended to be lower in chemoresistant (mean ± SEM: 113.45 ± 22.40 μg/mL) compared to chemosensitive patients (mean ± SEM: 145.07 ± 13.81 μg/mL), although this finding was not statistically significant ($p = 0.259$; Fig. 2A). This trend was also seen when comparing sEV-pGSN, although still with no statistically significant difference (mean ± SEM; sensitive: 639.45 ± 104.18 μg/mL; resistant: 355.46 ± 112.40 μg/mL. $p = 0.215$; Fig. 2B). When comparing receiver operating characteristic curves (ROC), the combination of total and sEV-pGSN showed a higher area under the curve (AUC) compared to each individual metric (combination: 0.591, total: 0.527, sEV: 0.543; Table 3). Despite these improved performance metrics for the combined pGSN prediction model, there was no statistically significant difference between these models (combined vs. total pGSN: $p = 0.575$; combined vs. sEV-pGSN: $p = 0.674$) (Table 4).

Predictive modelling of chemoresistance with MRI-based radiomics

Using MRI-based radiomic features, total pGSN, and sEV-pGSN, we generated predictive models of chemoresistance for all three MRI sequences and their combination (Fig. 3). The T2 with total and sEV-pGSN outperformed the ADC and PC models with higher sensitivity, specificity, and accuracy (Table 5). To better understand how the combination of features from different MRI sequences would impact the prediction algorithm, we repeated the machine learning with the selected sequence features. The T2 + ADC + PC model outperformed the ADC and PC models alone, but not the individual T2 model (Table 5). Given lower performance of the PC features alone in predicting chemoresistance, we generated a T2 + ADC model to avoid a combined model being negatively skewed by the PC features. This model performed similarly to its individual sequences. While the combined T2 + ADC + PC model was not statistically different from the T2 model alone ($p = 0.214$), the elevated AUC and fewer model parameters encouraged

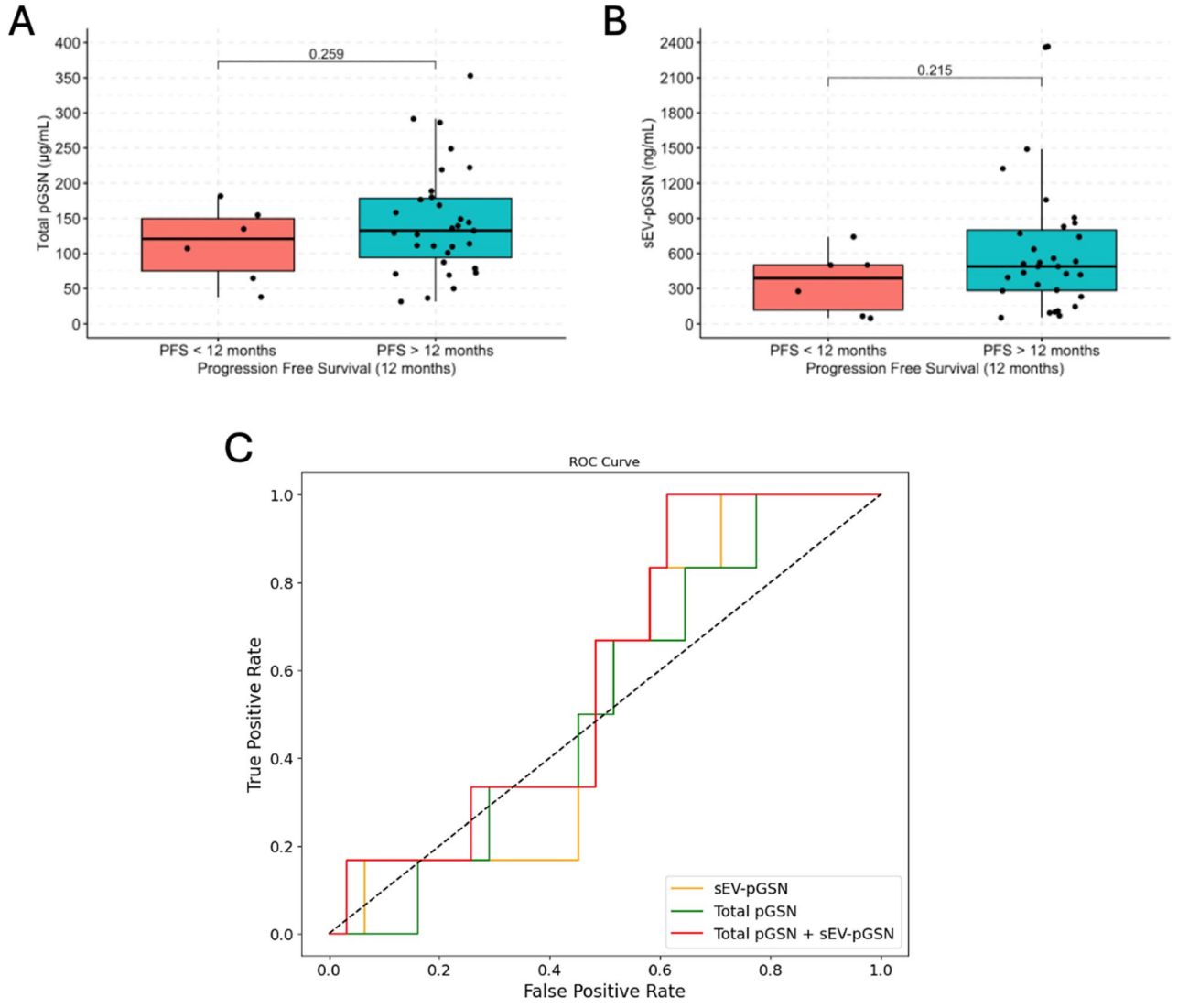

Fig. 2 Total and sEV-pGSN tend to be lower in chemoresistant patients. **A** Quantification of total pGSN from patient serum samples of chemosensitive (PFS > 12 months) and chemoresistant (PFS < 12 months) patients. **B** Quantification of sEV-pGSN from patient serum samples of chemosensitive and chemoresistant patients. **C** ROC curve comparing sensitivity and specificity of total pGSN, sEV-pGSN, and their combination

Table 3 Performance of pGSN and T2 radiomic models

Model	AUC	Sensitivity	Specificity	Accuracy
Total pGSN	0.527	0.720	0.417	0.474
sEV-pGSN	0.543	0.600	0.524	0.511
Total pGSN + sEV-pGSN	0.591	0.600	0.591	0.568
T2 only	0.903	0.790	0.903	0.885
T2 + total pGSN	0.919	0.790	0.927	0.905
T2 + sEV-pGSN	0.946	0.790	0.920	0.898
T2 + total pGSN + sEV-pGSN	0.973	0.833	0.968	0.946

our further analysis with the T2 model alone (Table 6). Compared to the combined total and sEV-pGSN prediction model, the inclusion of T2 radiomic features significantly improved the test performances, including AUC, sensitivity, specificity, and accuracy (Fig. 4A; Table 3). The combined model also outperformed the algorithm that considered T2 features alone, however not statistically significantly (Table 4).

Discussion

In this pilot exploratory study, we have demonstrated that the inclusion of MRI-based radiomics with circulating total and sEV-pGSN provides the best prediction of chemoresistance in EOC patients. Notably, the samples used in this investigation included serum collected from chemo-naïve patients and MRI scans taken at baseline and could help to guide therapeutic options in a first-line setting. It is anticipated that 80% of EOC patients will experience recurrence, and approximately one third of patients are resistant to first-line platinum-based chemotherapy [19, 20]. Therefore, a clinical tool to predict whether patients will respond to first line therapy could

Table 4 Statistical comparison of pGSN and T2 radiomic models

	T2 only	sEV-pGSN	Total pGSN	Total pGSN + sEV-pGSN	T2 + sEV-pGSN	T2 + total pGSN	T2 + total pGSN + sEV-pGSN
T2 only	NA						
sEV-pGSN	$p < 0.001$	NA					
Total pGSN	$p < 0.001$	0.889	NA				
Total pGSN + sEV-pGSN	$p < 0.001$	0.674	0.575	NA			
T2 + sEV-pGSN	0.482	$p < 0.001$	$p < 0.001$	$p < 0.001$	NA		
T2 + total pGSN	0.807	$p < 0.001$	$p < 0.001$	$p < 0.001$	0.644	NA	
T2 + total pGSN + sEV-pGSN	0.207	$p < 0.001$	$p < 0.001$	$p < 0.001$	0.556	0.302	NA

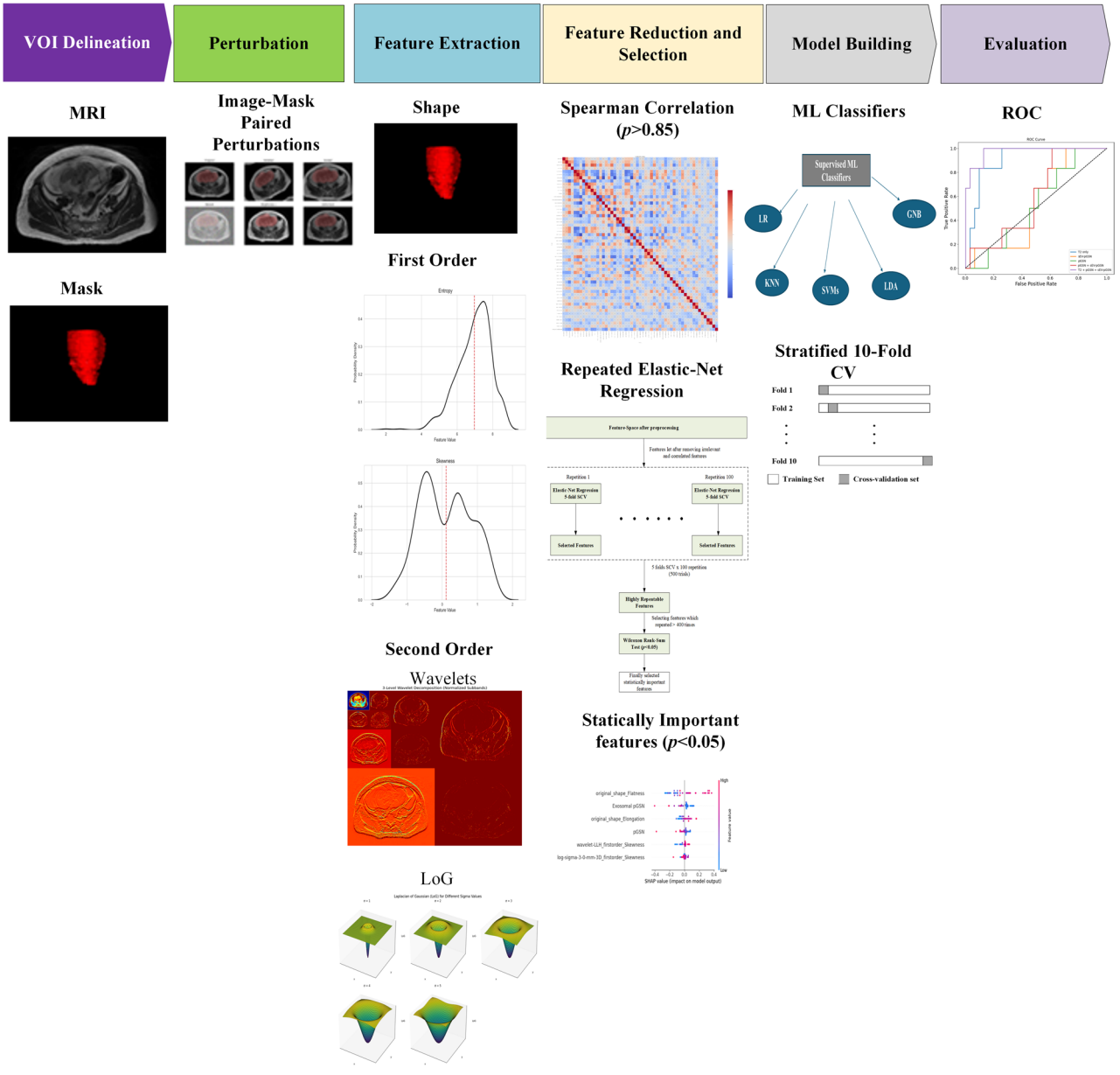

Fig. 3 Radiomics pipeline. Tumours from individual MR images were delineated and image perturbation was used to synthetically increase the sample size for feature extraction. Statistically important features for predicting chemoresistance were selected for model building. The performance of the model in predicting responsiveness to chemotherapy was evaluated

Table 5 Performance of radiomic models including total and sEV-pGSN. T2: T2-weighted imaging. ADC: apparent diffusion coefficient. PC: post contrast

Sequence	AUC	Sensitivity	Specificity	Accuracy	No. of model parameters
T2	0.973	0.833	0.968	0.946	6
ADC	0.914	0.880	0.822	0.831	7
PC	0.855	0.820	0.800	0.804	6
T2 + ADC	0.946	0.720	0.976	0.933	13
T2 + ADC + PC	0.941	0.840	0.960	0.940	8

Table 6 Statistical comparison of radiomic models including total and sEV-pGSN. T2: T2-weighted imaging. ADC: apparent diffusion coefficient. PC: post contrast

	T2	ADC	PC	T2 + ADC	T2 + ADC + PC
T2	N/A				
ADC	$p < 0.001$	N/A			
PC	$p < 0.001$	$p < 0.001$	N/A		
T2 + ADC	$p < 0.001$	$p < 0.001$	$p < 0.001$	N/A	
T2 + ADC + PC	0.214	0.058	$p < 0.001$	0.317	N/A

open doors to more personalized treatment with greater chance for treatment response.

We demonstrated that total circulating pGSN and sEV-pGSN tend to be lower in chemoresistant compared to chemosensitive patients in this cohort. In our previous study, we observed a decrease in total pGSN in chemoresistant patients [8], aligning well with our current results. We believe that this measure of pGSN is reflective tissue damage in the body. Several publications have indicated an association between decreased pGSN and increased disease severity, including in hospitalizations [21], sepsis [22], and COVID-19 [23]. Given the role of pGSN in actin clearance [22], it could be hypothesized that in the case of systemic tissue damage, pGSN might be depleted through clearance of actin. In alignment with this hypothesis, we found that tumour elongation and flatness were predictive of chemoresistance (Fig. 4B). There is an association between chemoresistance and aggressive tumours [24]. This relationship has also been observed in other radiomic studies. For example, both flatness and elongation were associated with invasiveness in bladder cancer [25]. Elongation was associated with Ki67 staining, a marker of cell proliferation, in lung tumours [26]. Moreover, in a CT-based radiomic study on omental lesions in high grade-serous EOC patients, elongation was positively associated with response to neoadjuvant chemotherapy [27]. Rapidly progressing and invasive tumours could increase damage to neighbouring healthy tissue, thus relating to decreased circulating pGSN. Ultimately, we propose that pGSN and these macroscopic radiomic features are complementary in their representation of disease severity, which is associated with chemoresistance. We believe this complementarily contributes to the improved prediction algorithm when pGSN and radiomic features are combined.

Contrary to our previous study, sEV-pGSN tended to be lower in chemoresistance patients in the current cohort, compared to increased sEV-pGSN in the prior cohort [8]. In our 2023 study, we proposed that increased sEV-pGSN in chemoresistant patients was reflective of chemoresistant EOC cells that secrete more pGSN in their EVs. A possible contributor to the opposing finding in this cohort is the use of serum samples, compared to the previous use of plasma. Serum is the liquid collected from blood after the sample has undergone coagulation, while plasma is the liquid collected from blood that was collected in the presence of an anticoagulant. During the coagulation process, platelets are known to secrete many EVs, which changes the composition of the EVs in in serum compared to plasma [28]. We expect that such an increase in overall EVs in the sample might overshadow those from the tumour and could explain the difference between study cohorts. Identifying the tumour-EVs in the isolated sEVs would allow us to better conclude the impact of using plasma or serum. Standardization of the sample type used in this assay will ensure the validity of the test result. Another notable difference between our studies is geographical location and therefore the ethnicity of included patients. A 2017 publication highlighted the different trends in incidence of different histological subtypes of EOC in different countries. Importantly, the rates of clear cell carcinoma is elevated in many Asian countries compared to Canada and the United States of America, where serous carcinoma is more common [29]. This is reflected in our own study cohorts, where the majority of patients from the Canadian study had serous EOC [8], but more than half of the Hong Kong cohort had clear cell carcinoma (Table 2). These differences in the composition of histological subtypes between studies could also contribute to the differences in results. A larger study population representing various ethnicities

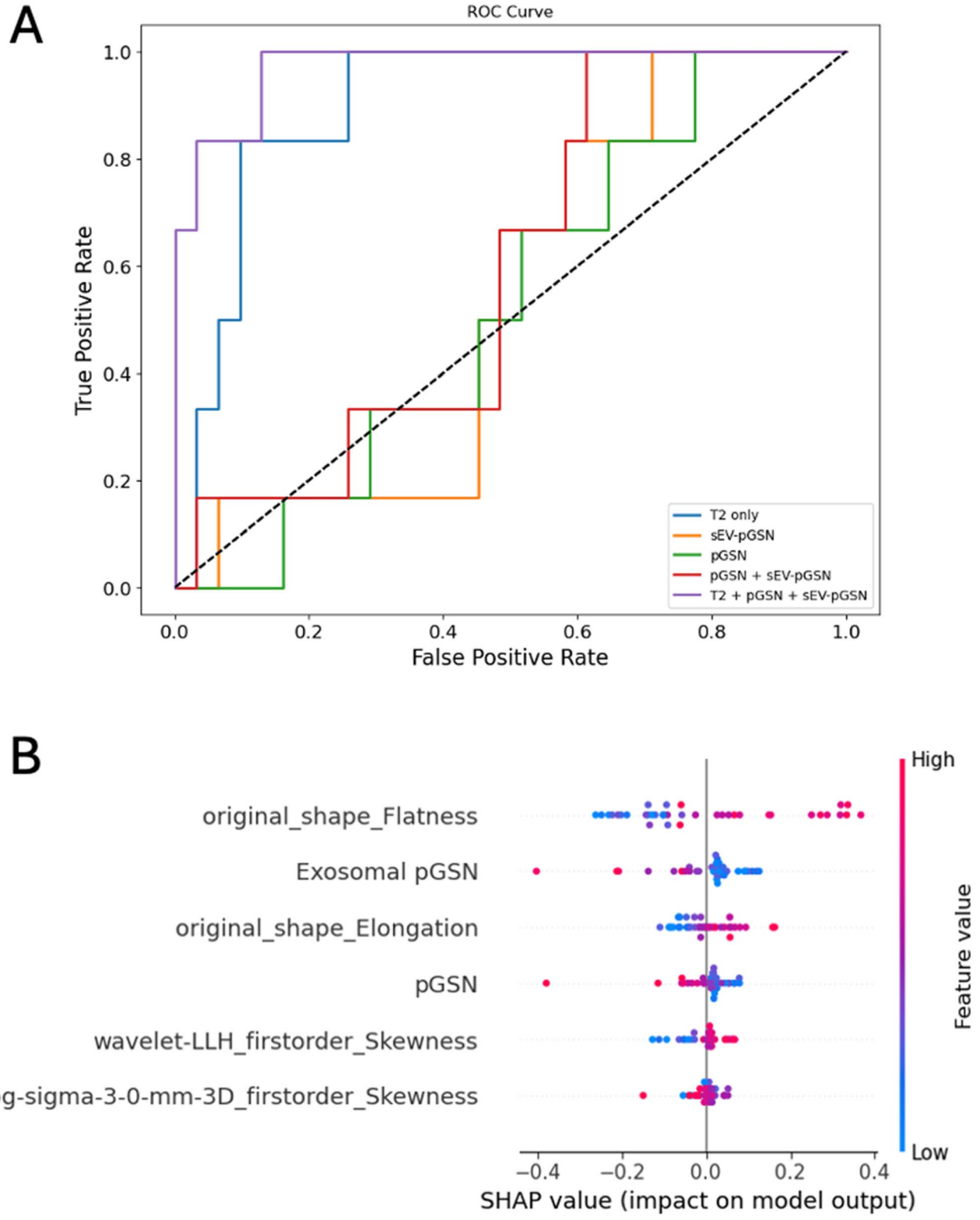

Fig. 4 The combination of T2 radiomics and total and sEV-pGSN have the best performance in predicting chemoresistance. **A** ROC curve comparing the sensitivity and specificity of total pGSN, sEV-pGSN, T2 radiomic features alone, and their combination. **B** SHAP (SHapley Additive exPlanations) values for variable included in the final T2 + total pGSN + sEV-pGSN model to predict chemoresponsiveness in EOC patients

and histologic subtypes could address possible differences between populations.

The greatest limitation of this study was the small sample size. When using large datasets, such as in radiomic analysis, it is important to use sufficiently large sample sizes for the results to be generalizable to a larger population. The consequence of a small sample size is possible overfitting, in which we cannot generalize our findings. To address this, we applied image perturbation for feature selection, allowing us to synthetically increase the sample size [30]. More specifically, we were able to increase our sample size 13-fold by generating MRI images that were slight deviations of the original, accounting for real-life variability. Additionally, when assessing the performance of the radiomics models, our selected model (T2-radiomics + total pGSN + sEV-pGSN) had fewer variables than the combined models. This further lowers the risk of overfitting by decreasing the computational complexity of the algorithm. Given the important risk of overfitting the model, we cannot conclude that the absolute values of the performance metrics of these models, such as AUC, sensitivity, or specificity, are translatable to a larger population. Rather, we hope to demonstrate the added value of considering both radiomic data and circulating biomarkers together to predict chemoresistance. To expand on this proof-of-concept study, a multicentre study with a larger sample size will enable us to more robustly apply machine learning and include internal and external validation sets, all while better representing heterogeneity in patient populations [31, 32].

Few published studies have investigated the use of MRI-based radiomics for predicting chemoresistance and infrequently to predict survival [33]. One recent example by Na et al. demonstrated that a prediction model combining radiomic features with clinical parameters improved performance of the prediction compared to radiomic features or clinical parameters alone [34]. Our results align well with this finding, in which we included both radiomic features and blood biomarkers in our best performing algorithm. Indeed, we included these circulating biochemical markers (CA125, total pGSN, and sEV-pGSN) in the feature selection process. As anticipated, CA125 was not selected as a statistically relevant variable in the model. This is not surprising, as many studies have shown that pre-treatment CA125 is not associated with chemoresistance (or survival, which is used to inform resistance clinically) in EOC patients [8, 35, 36]. Total and sEV-pGSN, however, were both selected with the radiomic features for inclusion in the prediction model. We found these to be influential variables for the algorithm's decision making.

In the best performing model (T2-radiomics + total pGSN + sEV-pGSN), we noted that the pGSN variables greatly enhanced the test specificity, improving our ability to capture those chemoresistant patients by decreasing the false-negative rate. These patients could be offered alternative therapeutic options or re-directed to clinical trials that they could benefit from, knowing that they are at risk of not responding to conventional platinum-based chemotherapy. It is important, however, to recognize the limitations in the translation of radiomic and EV-based biomarkers to clinical settings. Radiomic analysis is computationally demanding and requires expertise for data processing, which is time consuming. These challenges are being addressed by groups focused on automating steps in the radiomics pipeline, such as image segmentation [37, 38]. Likewise, EV isolation required to measure sEV-pGSN is a labour intensive, low-throughput process. To address this, development of microfluidics devices are enabling faster and more pure EV isolation along with biomarker detection [39]. Altogether, these ongoing research advancements will contribute to the successful translation of radiomic and EV-based biomarkers in clinical practice.

Conclusion

Taken all together, we have demonstrated that MRI-based radiomics showed promise to improve upon our prediction of chemoresistance in treatment-naïve EOC patients using total and sEV-pGSN in this pilot exploratory study. To the best of our knowledge, this is the first piece of literature using MRI radiomics in combination with circulating biomarkers to generate a predictive model of chemoresistance in EOC. We hope for this work to demonstrate the feasibility of generating a multiparametric algorithm that combines MRI-based radiomics with circulating biomarkers to predict chemoresistance. Our next steps will include building upon this in a prospective, multicentre study. Important considerations when establishing this study will be the standardization of the type of biospecimen collected, collection of additional genomic data (i.e., BRCA status), and automated segmentation methods. The incorporation of this type of tool into the clinic will be critical in guiding personalized treatment for patients.

Abbreviations

ADC	Apparent diffusion coefficient
AUC	Area under the curve
BSA	Bovine serum albumin
CA125	Cancer antigen 125
CCC	Clear cell carcinoma
CT	Computed tomography
CV	Cross validation
DWI	Diffusion weighted imaging
ECL	Enhanced chemiluminescence
ELISA	Enzyme-linked immunosorbent assay
EOC	Epithelial ovarian cancer
EV	Extracellular vesicle
FIGO	International federation of gynecology and obstetrics
GLCM	Gray level co-occurrence matrix
GLDM	Gray level dependence matrix

GLRLM	Gray level run length matrix
GLSZM	Gray level size zone matrix
GNB	Gaussian naïve bayes
HGSC	High-grade serous carcinoma
HRD	Homologous recombination deficiency
KNN	K-nearest neighbour
LDA	Least discriminant analysis
LR	Logistic regression
MRI	Magnetic resonance imaging
NGTDM	Neighbouring gray tone difference matrix
NTA	Nanoparticle tracking analysis
OD	Optical density
PBS	Phosphate buffered saline
PBST	Phosphate buffered saline-Tween 20
PC	Post contrast imaging
pGSN	Plasma gelsolin
PVDF	Polyvinylidene difluoride
RIPA	Radioimmunoprecipitation assay buffer
ROC	Receiver operating characteristic
SCV	Stratified cross validation
SDS	Sodium dodecyl sulfate
SEM	Standard error of mean
sEV	Small extracellular vesicle
SVM	Support vector machines
T2	T2-weighted imaging
TBST	Tris-buffered saline-Tween 20
TEM	Transmission electron microscopy
VOI	Volume of interest

Supplementary Information

The online version contains supplementary material available at https://doi.org/10.1186/s13048-025-01906-w.

Supplementary Material 1.

Clinical trial number

Not applicable.

Authors' contributions

EG, RS, BKT, EYPL, and KKLC conceived and designed the study. EG performed sEV isolation and ELISA. sEV characterization was performed and analyzed by EG, LC, ASTW and DB. sEV immunoelectron microscopy and analysis were performed by LC and ASTW. KKLC provided plasma samples. CNH and EYPL provided MRI scans. Segmentation of MRI scans was performed by EG and reviewed by EYPL. Radiomics analysis was performed by RS. EYPL and KKLC informed analysis and interpretation of clinical data. Statistical analyses were done by EG and RS. EG wrote the paper with scientific feedback from all authors. The authors read and approved the final manuscript.

Funding

This research was funded by the Hong Kong Health and Medical Research Fund (No. 03143616, awarded to EYPL) and the Canadian Institutes of Health Research (CIHR, ID PJT-168949, awarded to BKT). Furthermore, EG is a recipient of a Canada Graduate Scholarship-Doctoral Award and was awarded a Canada Graduate Scholarship-Michael Smith Foreign Study Supplement for the purpose of this study.

Data availability

The datasets used in this study are available from the corresponding author upon reasonable request.

Declarations

Ethics approval and consent to participate

Collection of human serum and MRI scans were approved by the Institutional Review Board of the University of Hong Kong/Hospital Authority Hong Kong West Cluster (IRB #UW11-298 and #UW18-607, respectively). Research was conducted in accordance with the Declaration of Helsinki. All work followed appropriate guidelines, and all patients provided written informed consent.

Competing interests

The authors declare no competing interests.

Author details

[1]Inflammation and Chronic Disease Program, Ottawa Hospital Research Institute, The Ottawa Hospital (General Campus), Ottawa, ON K1H 8L6, Canada
[2]Department of Cellular and Molecular Medicine, Faculty of Medicine, University of Ottawa, Ottawa, ON, Canada
[3]Department of Obstetrics and Gynaecology, School of Clinical Medicine, LKS Faculty of Medicine, University of Hong Kong, Hong Kong (SAR), People's Republic of China
[4]Department of Diagnostic Radiology, School of Clinical Medicine, LKS Faculty of Medicine, University of Hong Kong, Hong Kong (SAR), People's Republic of China
[5]School of Biological Sciences, University of Hong Kong, Hong Kong (SAR), People's Republic of China
[6]Department of Obstetrics and Gynecology, Faculty of Medicine, University of Ottawa, Ottawa, ON, Canada

Received: 26 May 2025 / Accepted: 10 November 2025
Published online: 25 November 2025

References

1. Lee S. Canadian Cancer Society. Chemotherapy for ovarian cancer. Available from: https://cancer.ca/en/cancer-information/cancer-types/ovarian/treatment/chemotherapy. Cited 31 Jan 2023.
2. Davis A, Tinker AV, Friedlander M. Platinum resistant ovarian cancer: what is it, who to treat and how to measure benefit? Gynecol Oncol. 2014;133(3):624–31.
3. Sturgeon CM, Duffy MJ, Stenman UH, Lilja H, Brünner N, Chan DW, et al. National academy of clinical biochemistry laboratory medicine practice guidelines for use of tumor markers in Testicular, Prostate, Colorectal, Breast, and ovarian cancers. Clin Chem. 2008;54(12):e11–79.
4. Zhu JW, Charkhchi P, Akbari MR. Potential clinical utility of liquid biopsies in ovarian cancer. Mol Cancer. 2022;21:114.
5. Plenderleith IH. Treating the treatment: toxicity of cancer chemotherapy. Can Fam Physician. 1990;36:1827–30.
6. Chang L, Ni J, Zhu Y, Pang B, Graham P, Zhang H, et al. Liquid biopsy in ovarian cancer: recent advances in circulating extracellular vesicle detection for early diagnosis and monitoring progression. Theranostics. 2019;9(14):4130–40.
7. Asare-Werehene M, Communal L, Carmona E, Le T, Provencher D, Mes-Masson AM, et al. Pre-operative circulating plasma Gelsolin predicts residual disease and detects early stage ovarian cancer. Sci Rep. 2019;9(1):13924.
8. Gerber E, Asare-Werehene M, Reunov A, Burger D, Le T, Carmona E, et al. Predicting chemoresponsiveness in epithelial ovarian cancer patients using circulating small extracellular vesicle-derived plasma Gelsolin. J Ovarian Res. 2023;16(1):14.
9. Asare-Werehene M, Nakka K, Reunov A, Chiu CT, Lee WT, Abedini MR, et al. The exosome-mediated autocrine and paracrine actions of plasma Gelsolin in ovarian cancer chemoresistance. Oncogene. 2020;39(7):1600–16.
10. Forstner R. CT and MRI in Ovarian Carcinoma. In: Hamm B, Forstner R, editors. MRI and CT of the Female Pelvis. Berlin, Heidelberg: Springer; 2007;233–63. Available from: https://doi.org/10.1007/978-3-540-68212-7_10. Cited 6 Jan 2025.
11. Gillies RJ, Kinahan PE, Hricak H. Radiomics: images are more than pictures, they are data. Radiology. 2016;278(2):563–77.
12. Jian J, Li Y, Pickhardt PJ, Xia W, He Z, Zhang R, et al. MR image-based radiomics to differentiate type I and type II epithelial ovarian cancers. Eur Radiol. 2021;31(1):403–10.
13. Wang M, Perucho JAU, Hu Y, Choi MH, Han L, Wong EMF, et al. Computed tomographic radiomics in differentiating histologic subtypes of epithelial ovarian carcinoma. JAMA Netw Open. 2022;5(12):e2245141.
14. Ruzicka M, Xiao F, Abujrad H, Al-Rewashdy Y, Tang VA, Langlois MA, et al. Effect of hemodialysis on extracellular vesicles and circulating submicron particles. BMC Nephrol. 2019;20(1):294.
15. Myette RL, Xiao F, Geier P, Feber J, Burger D, Kennedy CRJ. Urinary podocyte-derived large extracellular vesicles are increased in paediatric idiopathic nephrotic syndrome. Nephrol Dial Transplant. 2023;38(9):2089–91.

16. Yushkevich PA, Piven J, Hazlett HC, Smith RG, Ho S, Gee JC, et al. User-guided 3D active contour segmentation of anatomical structures: significantly improved efficiency and reliability. Neuroimage. 2006;31(3):1116–28.
17. van Griethuysen JJM, Fedorov A, Parmar C, Hosny A, Aucoin N, Narayan V, et al. Computational radiomics system to Decode the radiographic phenotype. Cancer Res. 2017;77(21):e104–7.
18. Whybra P, Zwanenburg A, Andrearczyk V, Schaer R, Apte AP, Ayotte A, et al. The image biomarker standardization initiative: standardized convolutional filters for reproducible radiomics and enhanced clinical insights. Radiology. 2024;310(2):e231319.
19. Board PATE, Ovarian, Epithelial. Fallopian Tube, and Primary Peritoneal Cancer Treatment (PDQ®). PDQ Cancer Information Summaries. National Cancer Institute (US); 2022. Available from: https://www.ncbi.nlm.nih.gov/books/NBK66007/. Cited 30 Nov 2022.
20. Lukanović D, Kobal B, Černe K. Ovarian cancer: treatment and resistance to pharmacotherapy. Reprod Med. 2022;3(2):127–40.
21. Peddada N, Sagar A, Ashish, Garg R. Plasma gelsolin: A general prognostic marker of health. Med Hypotheses. 2012;78(2):203–10.
22. Wang H, Cheng B, Chen Q, Wu S, Lv C, Xie G, et al. Time course of plasma gelsolin concentrations during severe sepsis in critically ill surgical patients. Crit Care. 2008;12(4):R106.
23. Asare-Werehene M, McGuinty M, Vranjkovic A, Galipeau Y, Cowan J, Cameron B, Cooper CL, Langlois M-A, Crawley AM and Tsang BK. Longitudinal profiles of plasma gelsolin, cytokines and antibody expression predict COVID-19 severity and hospitalization outcomes. Front Immunol. 2022;13:1011084. https://doi.org/10.3389/fimmu.2022.1011084.
24. Norouzi S, Gorgi Valokala M, Mosaffa F, Zirak MR, Zamani P, Behravan J. Crosstalk in cancer resistance and metastasis. Crit Rev Oncol Hematol. 2018;132:145–53.
25. Özdemir H, Azamat S, Sam Özdemir M. Can only the shape feature in radiomics help machine learning show that bladder cancer has invaded muscles? Cureus. 2023;15(9):e45488.
26. Zhou B, Xu J, Tian Y, Yuan S, Li X. Correlation between radiomic features based on contrast-enhanced computed tomography images and Ki-67 proliferation index in lung cancer: a preliminary study. Thorac Cancer. 2018;9(10):1235–40.
27. Rundo L, Beer L, Escudero Sanchez L, Crispin-Ortuzar M, Reinius M, McCague C, Sahin H, Bura V, Pintican R, Zerunian M, Ursprung S, Allajbeu I, Addley H, Martin-Gonzalez P, Buddenkotte T, Singh N, Sahdev A, Funingana I-G, Jimenez-Linan M, Markowetz F, Brenton JD, Sala E, Woitek R. Clinically Interpretable Radiomics-Based Prediction of Histopathologic Response to Neoadjuvant Chemotherapy in High-Grade Serous Ovarian Carcinoma. Front Oncol. 2022;12:868265. https://doi.org/10.3389/fonc.2022.868265.
28. Zhang X, Takeuchi T, Takeda A, Mochizuki H, Nagai Y. Comparison of serum and plasma as a source of blood extracellular vesicles: increased levels of platelet-derived particles in serum extracellular vesicle fractions alter content profiles from plasma extracellular vesicle fractions. PLoS One. 2022;17(6):e0270634.
29. Coburn S, Bray F, Sherman M, Trabert B. International patterns and trends in ovarian cancer incidence, overall and by histologic subtype. Int J Cancer. 2017;140(11):2451–60.
30. Zwanenburg A, Leger S, Agolli L, Pilz K, Troost EGC, Richter C, et al. Assessing robustness of radiomic features by image perturbation. Sci Rep. 2019;9(1):614.
31. Adusumilli P, Ravikumar N, Hall G, Swift S, Orsi N, Scarsbrook A. Radiomics in the evaluation of ovarian masses — a systematic review. Insights Imaging. 2023;14:165.
32. Huang ML, Ren J, Jin ZY, Liu XY, He YL, Li Y, et al. A systematic review and meta-analysis of CT and MRI radiomics in ovarian cancer: methodological issues and clinical utility. Insights Imaging. 2023;14:117.
33. Li HM, Gong J, Li RM, Xiao ZB, Qiang JW, Peng WJ, et al. Development of MRI-based radiomics model to predict the risk of recurrence in patients with advanced high-grade serous ovarian carcinoma. AJR Am J Roentgenol. 2021;217(3):664–75.
34. Na I, Noh JJ, Kim CK, Lee J-W, Park H. Combined radiomics-clinical model to predict platinum-sensitivity in advanced high-grade serous ovarian carcinoma using multimodal MRI. Front Oncol. 2024;14:1341228. https://doi.org/10.3389/fonc.2024.1341228.
35. Markman M, Federico M, Liu PY, Hannigan E, Alberts D. Significance of early changes in the serum CA-125 antigen level on overall survival in advanced ovarian cancer. Gynecol Oncol. 2006;103(1):195–8.
36. Wilbaux M, Hénin E, Oza A, Colomban O, Pujade-Lauraine E, Freyer G, et al. Prediction of tumour response induced by chemotherapy using modelling of CA-125 kinetics in recurrent ovarian cancer patients. Br J Cancer. 2014;110(6):1517–24.
37. Lin YC, Lin G, Pandey S, Yeh CH, Wang JJ, Lin CY, et al. Fully automated segmentation and radiomics feature extraction of hypopharyngeal cancer on MRI using deep learning. Eur Radiol. 2023;33(9):6548–56.
38. Wei H, Zheng T, Zhang X, Wu Y, Chen Y, Zheng C, et al. MRI radiomics based on deep learning automated segmentation to predict early recurrence of hepatocellular carcinoma. Insights Imaging. 2024;15(1):120.
39. Chen J, Zheng M, Xiao Q, Wang H, Chi C, Lin T, et al. Recent advances in Microfluidic-Based extracellular vesicle analysis. Micromachines (Basel). 2024;15(5):630.

Publisher's Note